Pergamon

PII: S0020-7225(96)00036-5

Int. J. Engng Sci. Vol. 34, No. 12, pp. 1423–1439, 1996
Copyright © 1996 Elsevier Science Ltd
Printed in Great Britain. All rights reserved
0020-7225/96 $15.00 + 0.00

SOLUTIONS FOR FLUID-PARTICLE FLOW AND HEAT TRANSFER IN A POROUS CHANNEL

ALI J. CHAMKHA

Mechanical Engineering Department, Kuwait University, Safat 13060, Kuwait

Abstract—Equations governing transient flow and heat transfer aspects of a particulate suspension with a constant finite volume fraction in a porous channel are developed. The steady-state problem is solved analytically and the transient problem is solved numerically by an iterative implicit finite difference scheme. The variations of the velocity and temperature profiles, volume flow rates, skin-friction coefficient, and the wall heat transfer coefficient with time and other physical parameters are illustrated graphically and discussed. Copyright © 1996 Elsevier Science Ltd.

1. INTRODUCTION

The importance of heat transfer between particulate suspension flows and solid surfaces is well known due to the occurrence of such flows in a wide host of industrial applications. The features of a steady single-phase flow in a porous channel with uniform suction and injection have been reported by White [1]. Ritter and Peddieson [2] presented unsteady solutions for two-phase flow in an impermeable channel. Recently, Chamkha [3] generalized the work of Ritter and Peddieson [2] to include particulate viscous effects and a hydromagnetic body force. It is of interest in this paper to consider transient flow of a particulate suspension with heat transfer in a porous channel. Understanding the effect of the presence of particles on the flow and heat transfer aspects of the problem requires the solution of the equations of motion for a two-phase fluid/particle system. Marble [4], Ishii [5] and Sha and Soo [6] have reported general continuum equations for simulating two-phase particulate suspension flows. These equations are sufficiently complex to preclude the possibility of exact solutions except in very idealized cases. Under steady-state conditions and for monodispersed spherical particles of constant density and constant suction (or injection) velocity and uniform properties, the convective terms in the governing equations reduce to simple linear terms which allow the equations to be solved in closed form.

Exact solutions are of great importance in multiphase flows because they can be used to check numerical solutions and to develop an understanding of limiting special cases. The purpose of this paper is to report steady-state analytical solutions and transient numerical solutions for the velocity and temperature profiles, volume flow rates, skin-friction coefficient and wall heat flux for flow of a two-phase particulate suspension in a porous channel with uniform suction and injection applied at the walls. The flow is generated by the application of a constant pressure gradient.

2. GOVERNING EQUATIONS

Consider incompressible, laminar, fully developed two-phase flow between two fixed infinite porous plates (or a channel) separated by a distance l. A constant pressure gradient exists in the x-direction. Let the lower plate be coincident with the plane $y = 0$ and the upper plate be placed at the plane $y = l$. The lower plate is held at a constant temperature T_0 and the upper plate at T_l. Uniform and equal fluid-phase suction and injection with velocity $V_w(>0)$ are

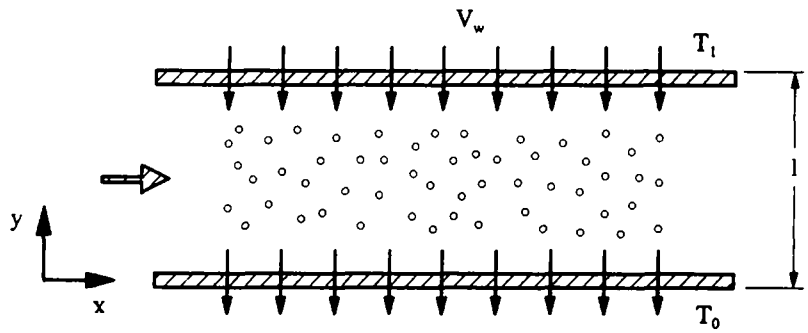

Fig. 1. Problem definition.

imposed at the lower and upper plates, respectively (see Fig. 1). Let the particle-phase Reynolds number be small (less than unity) with the volume fraction being finite and constant, and assume that the densities of both phases are constant.

The basic equations for the present investigation are based on the balance laws of mass, linear momentum, and energy for both phases which are viewed as interacting continua. In the present work, the hydrodynamic interaction of the particles and the fluid is restricted to a mutual drag force (based on Stoke's linear drag theory), whose value depends on the particle concentration and the relative velocity between the phases. Since the particle-phase Reynolds number is assumed to be small, other interaction forces such as the virtual mass force (Zuber [7]), the shear lift force (Saffman [8]), and the spin-lift force (Rubinow and Keller [9]) are negligible compared to the Stoke's drag force (Apazidis [10]). The thermal interaction between the phases is limited to energy transfer or heat flux due to temperature difference between the particles and the fluid. This depends on the ratio of the velocity relaxation time to the temperature relaxation time (Marble [4]). No radiative heat transfer from one particle to another and from mutual particle interaction is assumed to exist since the fluid acts as a buffer which prevents direct contacts between the surfaces of different particles. Models of this type have been given previously by many investigators (such as Marble [4] and Chamkha [11]) and can be written as

$$\left.\begin{aligned}
&\partial_t\phi - \vec{\nabla}\cdot((1-\phi)\vec{V}) = 0\\
&\partial_t\phi + \vec{\nabla}\cdot(\phi\vec{V}_p) = 0\\
&\rho(1-\phi)(\partial_t\vec{V} + \vec{V}\cdot\vec{\nabla}\vec{V}) = \vec{\nabla}\cdot\underline{\underline{\sigma}} - \vec{f}\\
&\rho_p\phi(\partial_t\vec{V}_p + \vec{V}_p\cdot\vec{\nabla}\vec{V}_p) = \vec{\nabla}\cdot\underline{\underline{\sigma}}_p + \vec{f}\\
&\rho c(1-\phi)(\partial_t T + \vec{V}\cdot\vec{\nabla}T) = k(1-\phi)\nabla^2 T + \underline{\underline{\sigma}}:\vec{\nabla}\vec{V} + Q_T + (\vec{V}-\vec{V}_p)\cdot\vec{f}\\
&\rho_p c_p\phi(\partial_t T_p + \vec{V}_p\cdot\vec{\nabla}T_p) = \underline{\underline{\sigma}}_p:\vec{\nabla}\vec{V}_p - Q_T
\end{aligned}\right\} \tag{2.1}$$

where

$$\left.\begin{aligned}
&\underline{\underline{\sigma}} = (1-\phi)(-p\underline{\underline{I}} + \mu(\phi)(\vec{\nabla}\vec{V} + \vec{\nabla}\vec{V}^T))\\
&\underline{\underline{\sigma}}_p = 0\\
&\vec{f} = \rho_p\phi(\vec{V} - \vec{V}_p)/\tau_v(\phi)\\
&Q_T = \rho_p c_p\phi(T_p - T)/\tau_T(\phi).
\end{aligned}\right\} \tag{2.2}$$

If the particle volume fraction is assumed to be small, equations (2.1) and (2.2) reduce to the original dusty-gas model given by Marble [4]. It should be noted herein that the effects of earth gravity are neglected. Soo [12] has shown that, compared with the effect of friction, gravity effects in pipe flow of a suspension are very small and, therefore, can be neglected.

Since the flow in the channel is fully developed in the x-direction, the flow physical variables

will only depend on the y coordinate and time. Upon taking into consideration the assumptions made above and substituting

$$\left.\begin{aligned} y &= l\eta \\ t &= (\rho l^2\tau)/\mu \\ \vec{V} &= \vec{e}_x V_c F(\tau,\eta) - \vec{e}_y V_w \\ \vec{V}_p &= \vec{e}_x V_c F_p(\tau,\eta) - \vec{e}_y V_w \\ dp/dx &= -(\mu V_c G)/l^2 \\ T &= (T_l - T_0)\theta(\tau,\eta) + T_0 \\ T_p &= (T_l - T_0)\theta_p(\tau,\eta) + T_0 \end{aligned}\right\} \tag{2.3}$$

into equations (2.1) and (2.2), the governing equations reduce to

$$\partial_\tau F - \partial_{\eta\eta} F - \mathrm{Re}_w \partial_\eta F - \kappa\alpha(F_p - F) - G = 0 \tag{2.4}$$

$$\partial_\tau F_p - \mathrm{Re}_w \partial_\eta F_p - \alpha(F - F_p) = 0 \tag{2.5}$$

$$\mathrm{P}_r\partial_\tau\theta - \partial_{\eta\eta}\theta - \mathrm{Re}_w\mathrm{P}_r\partial_\eta\theta - \kappa\mathrm{P}_r\gamma\epsilon(\theta_p - \theta) - E_c\mathrm{P}_r(\partial_\eta F)^2 - E_c\mathrm{P}_r\kappa\alpha(F_p - F)^2 = 0 \tag{2.6}$$

$$\partial_\tau\theta_p - \mathrm{Re}_w\partial_\eta\theta_p - \epsilon(\theta - \theta_p) = 0 \tag{2.7}$$

where

$$\left.\begin{aligned} \mathrm{Re}_w &= (\rho V_w l)/\mu \\ \kappa &= (\rho_p\phi)/(\rho(1-\phi)) \\ \alpha &= (\rho l^2)/(\mu\tau_v) \\ \mathrm{P}_r &= (\mu c)/k \\ \gamma &= c_p/c \\ \epsilon &= (\rho l^2)/(\mu\tau_T) \\ E_c &= V_c^2/(c(T_l - T_0)) \end{aligned}\right\} \tag{2.8}$$

In equation (2.5) the last term represents the drag force between the phases. The last three terms of equation (2.6) represent interphase energy or heat flux, viscous dissipation, and work or heat dissipation due to relative motion of the phases, respectively. It is seen, as mentioned earlier, that the motion of both phases are coupled through drag and heat transfer between them.

The corresponding nondimensional initial and boundary conditions for this problem are

$$F(0,\eta) = 0,\ F_p(0,\tau) = 0,\ F(\tau,0) = 0,\ F(\tau,1) = 0,\ \partial_\eta F_p(\tau,1) = 0, \tag{2.9}$$

$$\theta(0,\eta) = 0,\ \theta_p(0,\eta) = 0,\ \theta(\tau,0) = 0,\ \theta(\tau,1) = 1,\ \partial_\eta\theta_p(\tau,1) = 0. \tag{2.10}$$

It should be pointed out that the exact form of boundary conditions to be used for a particle phase at a surface is not known at present. The governing equations for the particle phase are often evaluated at the wall and employed in place of boundary conditions. However, when this is done in the present problem, a physically unacceptable solution arises, in which particle phase backflow occurs. This was also predicted by Tsuo and Gidaspow [13] for pipe flow. Tsuo and Gidaspow [13] mention that in this case a boundary for the solids must be prescribed at the wall. After some experimentation with different boundary conditions, it was decided to use a no-slip condition for the particle phase at the upper wall (which implies from equation (2.5) that the slope of the particle velocity at the upper wall must vanish). This seems to give a reasonable solution without any difficulties. This type of boundary condition was arrived at by endowing the particle phase by the so-called particle-phase viscosity (which yields a second derivative of F_p with respect to the η term in the governing equations [13, 14]), using a

boundary condition similar to that used for a rarefied gas (see, for instance, Soo [12] and Tsuo and Gidaspow [13]) and taking the limit as the particle-phase viscosity approaches zero.

Of special interest in this type of problem are the fluid-phase volume flow rate, the particle-phase volume flow rate, the fluid-phase skin-friction coefficient at the lower wall, and the heat flux coefficient at the lower wall. These can be defined, respectively, as

$$\left.\begin{aligned} Q(\tau) &= \int_0^1 F(\tau,\eta)\mathrm{d}\eta \\ Q_\mathrm{p}(\tau) &= \int_0^1 F_\mathrm{p}(\tau,\eta)\mathrm{d}\eta \\ C(\tau) &= -\partial_\eta F(\tau,0) \\ q_\mathrm{w}(\tau) &= -\partial_\eta \theta(\tau,0)/(\mathrm{P_r}E_\mathrm{c}\mathrm{Re_w}) \end{aligned}\right\} \tag{2.11}$$

where the negative signs in the last two equations indicate that friction is opposite to the direction of motion and that the direction of the heat flux is toward the lower wall of the channel since it is kept at a temperature lower than that of the fluid moving above it. Similar expressions for the fluid-phase skin-friction and heat flux coefficients can be defined at the upper plate of the channel. This is, however, not done here, for brevity and to prevent confusion with those properties associated with the lower plate. It should also be mentioned that since the temperature of the upper plate is maintained higher than that of the fluid in the channel, heat will be transferred from the upper plate to the fluid.

3. RESULTS AND DISCUSSION

In this section exact solutions for the flow and heat transfer aspects in the porous channel under steady-state conditions and numerical solutions for the transient conditions will be reported. Then, graphical results of various physical parameters will be presented and discussed in detail to illustrate special characteristics of this kind of suspension flow.

3.1 Steady-state solutions

The transport of particulate suspensions in channels and ducts excluding startups and shutdowns can be considered as steady-state operations. This type of operation is considered in this section. Since the flow is incompressible, the solution for the hydrodynamic problem (represented by the fluid- and particle-phase momentum equations) is uncoupled from the thermal problem (represented by the fluid- and particle-phase energy equations) and, therefore, its solution can be obtained first. Then, this solution can be used in solving the thermal problem. The steady-state conditions are attained when all the physical variables are no longer dependent on time. This occurs at large values of τ. Thus, the steady-state equations for the problem under investigation are obtained by setting all the derivatives with respect to τ equal to zero. If this is done, one obtains

$$F'' + \mathrm{Re_w}F' + \kappa\alpha(F_\mathrm{p} - F) + G = 0 \tag{3.12}$$

$$\mathrm{Re_w}F_\mathrm{p}' + \alpha(F - F_\mathrm{p}) = 0 \tag{3.13}$$

$$\theta'' + \mathrm{Re_w}\mathrm{P_r}\theta' + \kappa\mathrm{P_r}\gamma\epsilon(\theta_\mathrm{p} - \theta) + E_\mathrm{c}\mathrm{P_r}(F')^2 + E_\mathrm{c}\mathrm{P_r}\kappa\alpha(F_\mathrm{p} - F)^2 = 0 \tag{3.14}$$

$$\mathrm{Re_w}\theta_\mathrm{p}' + \epsilon(\theta - \theta_\mathrm{p}) = 0 \tag{3.15}$$

where a prime denotes ordinary differentiation with respect to η.

Combining equations (3.12) and (3.13) into a third-order, linear, differential equation in F gives

$$F''' + AF'' + BF' - (\alpha G)/\mathrm{Re}_w = 0 \tag{3.16}$$

where

$$A = (\mathrm{Re}_w^2 - \alpha)/\mathrm{Re}_w,\ B = -\alpha(1+\kappa). \tag{3.17}$$

Equation (3.16) can be solved subject to the flow boundary conditions given in equations (2.9) by the usual method of solving such equations to give

$$F = \frac{(\alpha G)\eta}{(\mathrm{Re}_w B)} + C_2(\exp(m_2\eta) - 1) + C_3(\exp(m_3\eta) - 1) \tag{3.18}$$

where

$$m_2 = \frac{-A - (A^2 - 4B)^{1/2}}{2}, \qquad m_3 = \frac{-A + (A^2 - 4B)^{1/2}}{2}$$

$$C_3 = -(\alpha G)/(\mathrm{Re}_w B)(1 - (1 - m_2(1 - m_2/(\kappa\alpha)(\mathrm{Re}_w + m_2)))\exp(m_2))/(m_3(1 - m_3/(\kappa\alpha)$$
$$\times(\mathrm{Re}_w + m_3))\exp(m_3)(1 - \exp(m_2)) - m_2(1 - m_2/(\kappa\alpha)(\mathrm{Re}_w + m_2))\exp(m_2)(1 - \exp(m_3)))$$

$$C_2 = -((\alpha G)/(\mathrm{Re}_w B) + C_3 m_3(1 - m_3/(\kappa\alpha)(\mathrm{Re}_w + m_3))\exp(m_3))/(m_2(1 - m_2/(\kappa\alpha)$$
$$\times(\mathrm{Re}_w + m_2))\exp(m_2)). \tag{3.19}$$

The solution for F_p is then obtained and is given by

$$F_p = \frac{G}{B}(1 + \alpha/\mathrm{Re}_w\eta) + C_2\{[1 - m_2/(\kappa\alpha)(\mathrm{Re}_w + m_2)]\exp(m_2\eta) - 1\}$$
$$+ C_3\{[1 - m_3/(\kappa\alpha)(\mathrm{Re}_w + m_3)]\exp(m_3\eta) - 1\}. \tag{3.20}$$

Since F and F_p are known, the volume flow rates of both the fluid and the particle phases (Q and Q_p) as well as the skin-friction coefficient C at the lower plate can now be determined. This can be accomplished by substituting F, F_p, and the first derivative of F evaluated at $\eta = 0$ into the expressions for Q, Q_p, and C of equations (2.11) and integrating within the flow area between the lower plate at $\eta = 0$ and the upper plate at $\eta = 1$ (for Q and Q_p) to yield

$$Q = (\alpha G)/(2\mathrm{Re}_w B) + \frac{C_2(\exp(m_2) - m_2 - 1)}{m_2} + \frac{C_3(\exp(m_3) - m_3 - 1)}{m_3}$$

$$Q_p = \frac{G(1 + \alpha/(2\mathrm{Re}_w))}{B} + C_2\{[1 - m_2/(\kappa\alpha)(\mathrm{Re}_w + m_2)][\exp(m_2) - 1]/m_2 - 1\}$$
$$+ C_3\{[1 - m_3/(\kappa\alpha)(\mathrm{Re}_w + m_3)][\exp(m_3) - 1]/m_3 - 1\}$$

$$C = -((\alpha G)/(\mathrm{Re}_w B) + C_2 m_2 + C_3 m_3). \tag{3.21}$$

With the solutions for the flow problem known, the solution for the thermal problem can now be obtained from equations (3.14) and (3.15). Solving for θ_p from equation (3.14), then differentiating once and substituting the results into equation (3.15) yields a third-order differential equation in θ. This can be rearranged and written as

$$\theta''' + X\theta'' + Y\theta' + E_c P_r((F')^2)' + E_c P_r \kappa\alpha((F_p - F)^2)' - \frac{E_c P_r \epsilon (F')^2}{\mathrm{Re}_w} - \frac{E_c P_r \kappa\alpha\epsilon(F_p - F)^2}{\mathrm{Re}_w} = 0$$

$$X = (\mathrm{Re}_w^2 P_r - \epsilon)/\mathrm{Re}_w \qquad Y = -P_r\epsilon(1 + \kappa\gamma) \tag{3.22}$$

The solution for the above equation subject to the boundary conditions given earlier [equations (2.10)] after employing the results for F and F_p can be shown to be

$$\theta = C_5 + A_{11}(\eta - X) + C_6\exp(s_2\eta) + C_7\exp(s_3\eta) + A_6\exp(m_2\eta) + A_7\exp(m_3\eta) + A_8\exp(2m_2\eta) + A_9\exp(2m_3\eta) + A_{10}\exp((m_2+m_3)\eta) \tag{3.23}$$

where

$$\left.\begin{aligned} A_{11} &= \frac{E_c P_r \epsilon G^2(\alpha^2/(\mathrm{Re}_w^2 B^2) + (1+\alpha/B)^2)}{(\kappa\alpha)/(\mathrm{Re}_w Y)} \\ A_6 &= \frac{2C_2 m_2 E_c P_r G(\epsilon/\mathrm{Re}_w - m_2)(\alpha - \mathrm{Re}_w(\mathrm{Re}_w + m_2))}{\mathrm{Re}_w B m_2(m_2^2 + Xm_2 + Y)} \\ A_7 &= \frac{2C_3 m_3 E_c P_r G(\epsilon/\mathrm{Re}_w - m_3)(\alpha - \mathrm{Re}_w(\mathrm{Re}_w + m_3))}{\mathrm{Re}_w B m_3(m_3^2 + Xm_3 + Y)} \end{aligned}\right\} \tag{3.24}$$

$$\left.\begin{aligned} A_8 &= \frac{C_2^2 m_2^2 E_c P_r(\epsilon/\mathrm{Re}_w - 2m_2)(1 + (\mathrm{Re}_w + m_2)^2/(\kappa\alpha))}{2m_2(4m_2^2 + 2Xm_2 + Y)} \\ A_9 &= \frac{C_3^2 m_3^2 E_c P_r(\epsilon/\mathrm{Re}_w - 2m_3)(1 + (\mathrm{Re}_w + m_3)^2/(\kappa\alpha))}{2m_3(4m_3^2 + 2Xm_3 + Y)} \\ A_{10} &= \frac{2C_2 C_3 m_2 m_3 E_c P_r(\epsilon/\mathrm{Re}_w - m_2 - m_3)(1 + (\mathrm{Re}_w + m_2)(\mathrm{Re}_w + m_3)/(\kappa\alpha))}{(m_2+m_3)((m_2+m_3)^2 + X(m_2+m_3) + Y)} \end{aligned}\right\} \tag{3.25}$$

$$\left.\begin{aligned} C_7 &= -A_{17}(\exp(s_2) - 1) + \frac{A_{18}s_2(1 - s_2(s_2 + P_r\mathrm{Re}_w)/(\kappa\epsilon P_r\gamma))\exp(s_2)}{A_{19}} \\ C_6 &= \frac{A_{18} - C_7(\exp(s_3) - 1)}{\exp(s_2) - 1} \\ C_5 &= -(C_6 + C_7 + A_6 + A_7 + A_8 + A_9 + A_{10}) + XA_{11} \end{aligned}\right\} \tag{3.26}$$

$$\left.\begin{aligned} A_{17} &= m_2A_{12}\exp(m_2) + m_3A_{13}\exp(m_3) + 2m_2A_{14}\exp(2m_2) + 2m_3A_{15}\exp(2m_3) \\ &\quad + (m_2+m_3)A_{16}\exp m_2 + m_3 \\ A_{18} &= 1 + A_6(1 - \exp(m_2)) + A_7(1 - \exp(m_3)) + A_8(1 - \exp(2m_2)) + A_9(1 - \exp(2m_3)) \\ &\quad + A_{10}(1 - \exp(m_2 + m_3)) - A_{11} \\ A_{19} &= s_3[1 - s_3(s_3 + P_r\mathrm{Re}_w)/(\kappa\epsilon P_r\gamma)]\exp(s_3)[\exp(s_2) - 1] \\ &\quad - s_2[1 - s_2(s_2 + P_r\mathrm{Re}_w)/(\kappa\epsilon P_r\gamma)]\exp(s_2)[\exp(s_3) - 1] \end{aligned}\right\} \tag{3.27}$$

$$\left.\begin{aligned} A_{12} &= A_6[1 - m_2(m_2 + P_r\mathrm{Re}_w)/(\kappa\epsilon P_r\gamma)] - \frac{2C_2 m_2 E_c G(\alpha/\mathrm{Re}_w - (\mathrm{Re}_w + m_2))}{\kappa\epsilon\gamma B} \\ A_{13} &= A_7[1 - m_3(m_3 + P_r\mathrm{Re}_w)/(\kappa\epsilon P_r\gamma)] - \frac{2C_3 m_3 E_c G(\alpha/\mathrm{Re}_w - (\mathrm{Re}_w + m_3))}{\kappa\epsilon\gamma B} \\ A_{14} &= A_8[1 - 2m_2(2m_2 + P_r\mathrm{Re}_w)/(\kappa\epsilon P_r\gamma)] - \frac{C_2^2 m_2^2 E_c(1 + (\mathrm{Re}_w + m_2)^2/(\kappa\alpha))}{\kappa\epsilon\gamma} \end{aligned}\right\} \tag{3.28}$$

$$\left.\begin{aligned} A_{15} &= A_9[1 - 2m_3(2m_3 + P_r\mathrm{Re}_w)/(\kappa\epsilon P_r\gamma)] - \frac{C_3^2 m_3^2 E_c(1 + (\mathrm{Re}_w + m_3)^2/(\kappa\alpha))}{\kappa\epsilon\gamma} \\ A_{16} &= A_{10}[1 - (m_2+m_3)(m_2 + m_3 + P_r\mathrm{Re}_w)/(\kappa\epsilon P_r\gamma)] \\ &\quad - \frac{2C_2 C_3 m_2 m_3 E_c(1 + (\mathrm{Re}_w + m_2)(\mathrm{Re}_w + m_3)/(\kappa\alpha))}{\kappa\epsilon\gamma}. \end{aligned}\right\} \tag{3.29}$$

The corresponding solution for θ_p can be written as

$$\theta_p = C_5 + A_{11}(\eta - X - \mathrm{Re}_w/(\kappa\epsilon\gamma)) - \frac{E_c G^2(\alpha^2/(\mathrm{Re}_w^2 B^2) + (1+\alpha/B)^2/(\kappa\alpha))}{\kappa\epsilon\gamma}$$
$$+ C_6[1 - s_2(s_2 + \mathrm{P_r Re}_w)/(\kappa\epsilon \mathrm{P_r}\gamma)]\exp(s_2\eta)$$
$$+ C_7[1 - s_3(s_3 + \mathrm{P_r Re}_w)/(\kappa\epsilon \mathrm{P_r}\gamma)]\exp(s_3\eta) + A_{12}\exp(m_2\eta) + A_{13}\exp(m_3\eta)$$
$$+ A_{14}\exp(2m_2\eta) + A_{15}\exp(2m_3\eta) + A_{16}\exp((m_2+m_3)\eta). \tag{3.30}$$

The heat transfer coefficient q_w at the lower wall of the channel can be found by differentiating equation (3.23) once, evaluating it at $\eta = 0$, and then substituting the result into the last equation of (2.11). If this is done, one obtains

$$q_w = \frac{C_6 s_2 + C_7 s_3 + m_2(A_6 + 2A_8 + A_{10}) + m_3(A_7 + 2A_9 + A_{10}) + A_{11}}{\mathrm{P_r} E_c \mathrm{Re}_w}. \tag{3.31}$$

It should be pointed out that, unlike most exact solutions currently available for two-phase flow, the present results are not limited to small particulate volume fraction. It should be remembered that the existence of the closed-form solutions presented earlier is due to the relative simplicity introduced by assuming that the particle volume fraction is constant. It should be mentioned that, in practice, there are very limited cases where the particle volume fraction can be considered uniform such as in slow filtration, but this assumption is necessary to obtain closed-form solutions that can be used to check the numerical solutions of the transient problem. There are more elaborate constitutive theories which predict non-uniform particle volume fraction (see, for instance, Drew and Lahey [15], Sinclair and Jackson [16], and Wang *et al.* [17]). As shown by Sinclair and Jackson [16], the inclusion of a lift force in the interphase force is sufficient (but not necessary) to produce non-uniform particle-phase volume fraction distribution. It is, obviously, not possible to obtain exact solutions in this case.

Figures 2–9 are shown to illustrate the steady behavior of the velocity and temperature profiles for both phases, the fluid and particulate volume flow rates, and the fluid-phase skin-friction coefficient and wall heat transfer for a constant pressure gradient $G = 1.0$. These figures are obtained by numerically evaluating the exact solutions for F, F_p, θ, θ_p, Q, Q_p, C, and q_w for various parametric values. To provide a check on the correctness of these results, an implicit finite-difference solution of the governing equations was also obtained. The numerical algorithm will be discussed in the next section. The numerical results are represented by the markers on Figs 4, 5, 6 and 9. It should be pointed out that each marker requires a separate calculation. It is apparent that the numerical results are in excellent agreement with the exact solutions. These comparisons lend confidence in the numerical scheme employed in the present work.

Figures 2 and 3 present representative velocity profiles for the fluid and particle phases in the porous channel for different particle loading or concentration level, respectively. As expected, higher particle concentration level yields lower fluid and particle velocity distributions in the channel. This is clearly the case as shown in Figs 2 and 3. Figure 3 shows that for any value of κ, the particle phase is predicted to have some amount of wall slip at the lower channel boundary as often observed in real situations.

Figures 4, 5 and 6 demonstrate the variations in the fluid-phase volume flow rate Q, the particle-phase volume flow rate Q_p, and the fluid-phase skin-friction coefficient C that are brought about by changes in both the velocity inverse Stokes number α and the particle loading κ, respectively. As mentioned earlier, increases in the particle loading cause reduction in the

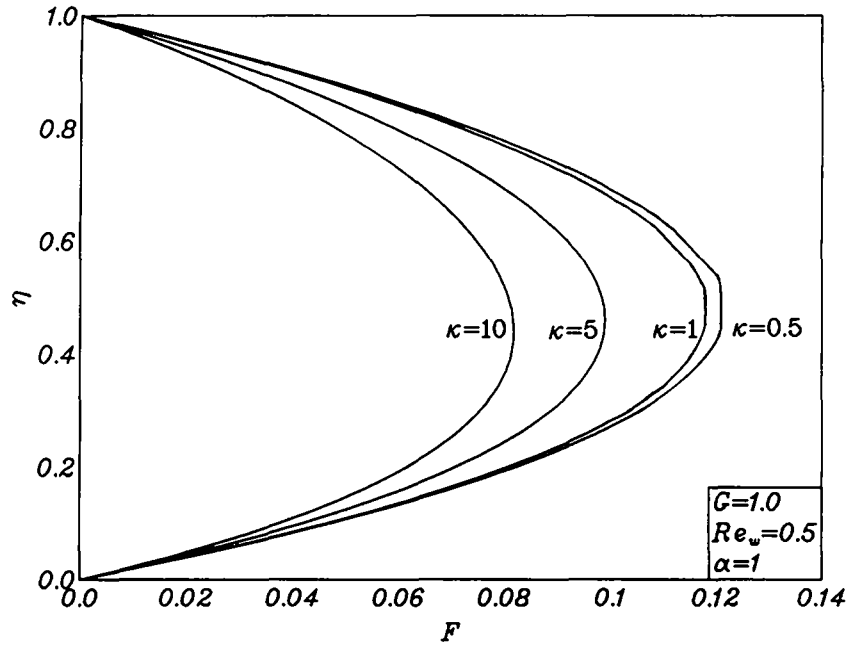

Fig. 2. Fluid-phase velocity profiles.

fluid and particle velocities. This, in turn, causes Q and Q_p to decrease as predicted by Figs 4 and 5. Increasing in the values of α have the tendency to increase the coupling between the phases through the drag force causing Q and C to decrease and Q_p to increase as is evident from Figs 4–6. At large values of α, equilibrium conditions between the phases occur in which both phases move together with the same velocity. These conditions are illustrated by the dashed lines on these figures. For large values of κ and moderate values of α, Figs 4 and 6 suggest the existence of a minimum in the values of Q and C and then a fast upward trend in approaching the equilibrium limits. This effect is more pronounced for large particle loading.

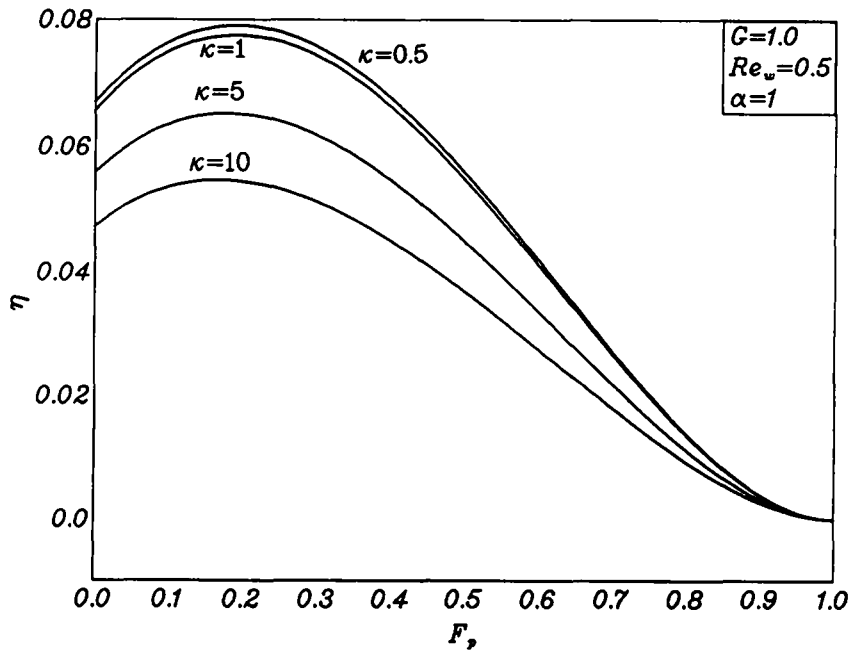

Fig. 3. Particle-phase velocity profiles.

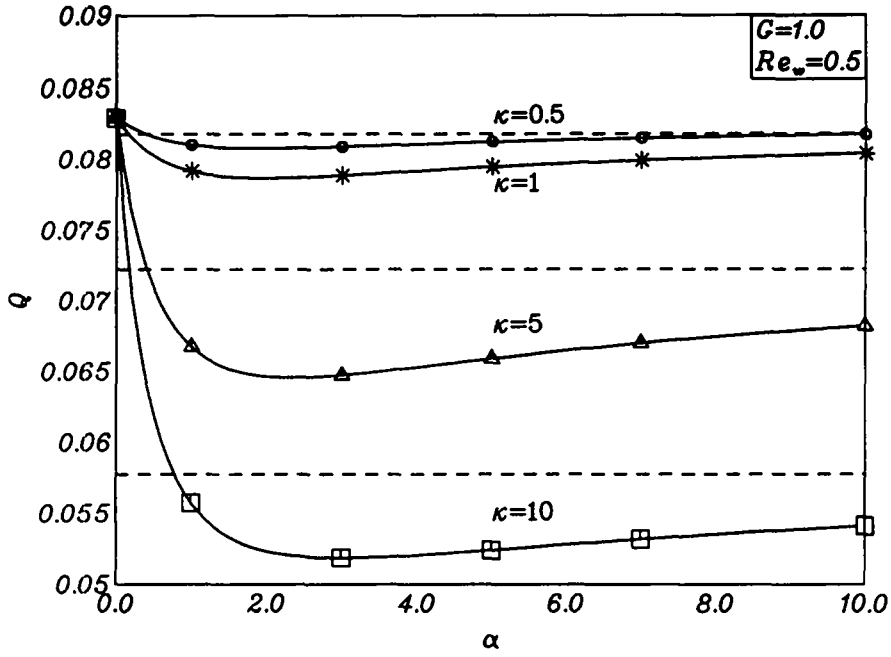

Fig. 4. Fluid-phase volume flow rate vs. α.

This type of behavior was also observed in the case of fluid-particle flow in an impermeable channel [3].

Figures 7 and 8 show representative temperature profiles for the fluid and particle phases in the channel for various values of the particle loading κ, respectively. Increasing κ causes the temperatures of both phases to increase. Figure 9 elucidates the effect of the particle loading κ and the temperature inverse Stokes number ϵ on the lower wall heat transfer coefficient q_w. The increase in the fluid-phase temperature as a result of increasing κ causes the slope of temperature profile at the lower wall of the channel to increase. This results in an increase in

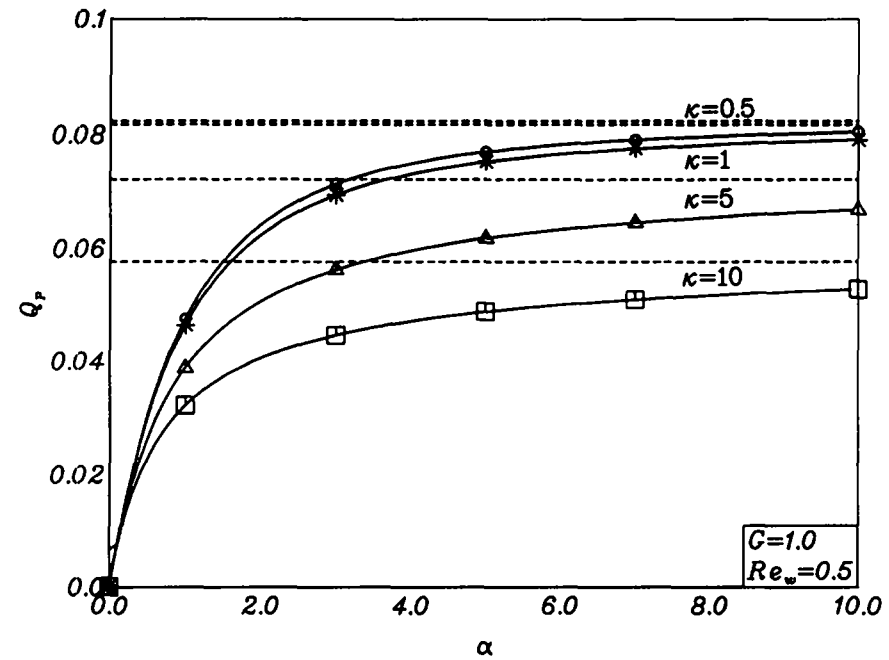

Fig. 5. Particle-phase volume flow rate vs. α.

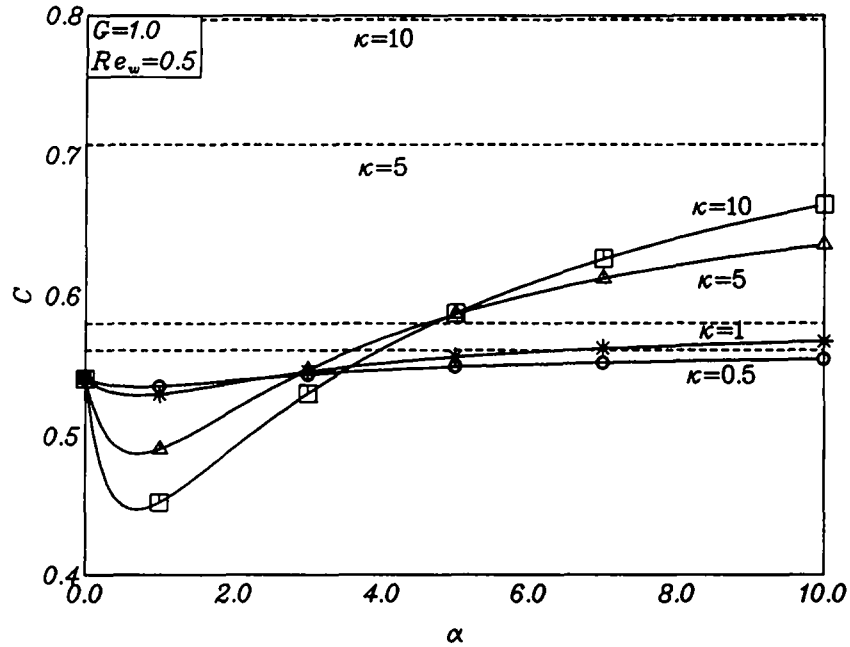

Fig. 6. Fluid-phase skin-friction coefficient vs α.

the values of q_w. Increases in the temperature inverse Stokes number ϵ have the tendency to increase the interphase energy transfer between the phases which, in turn, increases the slope of the fluid-phase temperature at the lower plate. This causes q_w to increase with increasing ϵ as evident from Fig. 9. The dashed lines on this figure indicate the thermal equilibrium limit reached at large values of ϵ. In the absence of particles ($\kappa = 0$), the predicted results are in close agreement with those given by White [1].

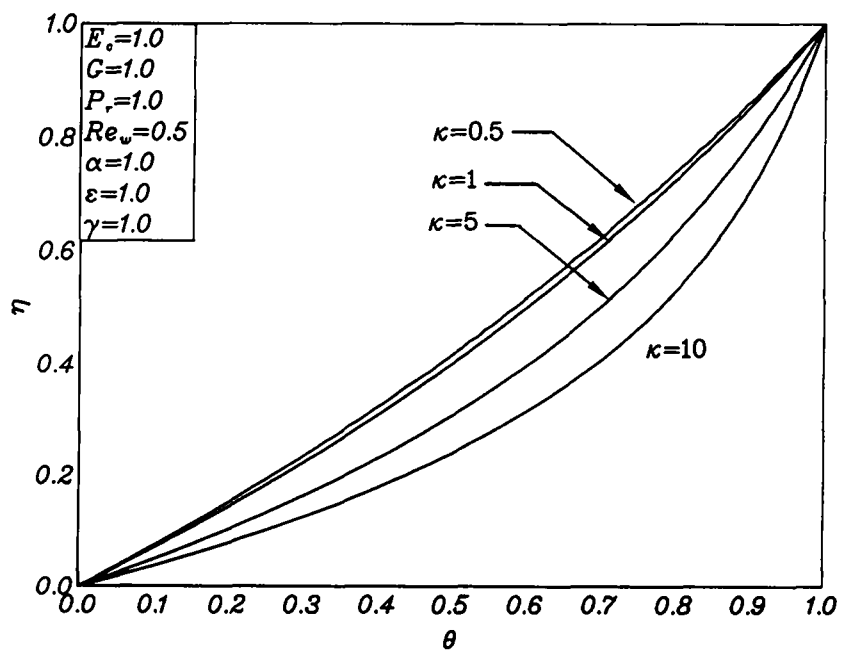

Fig. 7. Fluid-phase temperature profiles.

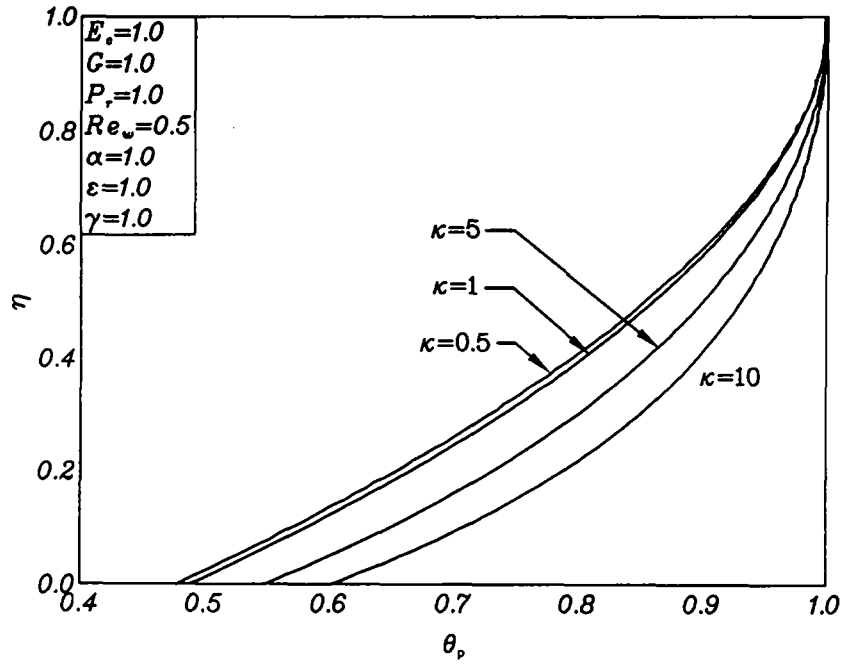

Fig. 8. Particle-phase temperature profiles.

3.2 *Transient solutions*

Numerical results of equations (2.4)–(2.7) subject to equations (2.9) and (2.10) were computed using an extension of the implicit finite-difference method similar to that discussed by Patankar [18] and described by Blottner [19] to two-phase flow. A 1000×201 grid (in τ and η, respectively) was utilized. Constant step sizes in η ($\Delta\eta = 0.005$) and variable step sizes in τ (with the smallest step size ($\Delta\tau_1 = 0.001$) at the initial start of motion when significant variations in results could occur) were employed. A growth factor of 1.03 was used in the τ direction. It should be mentioned that the step sizes used in the present work were chosen as a result of

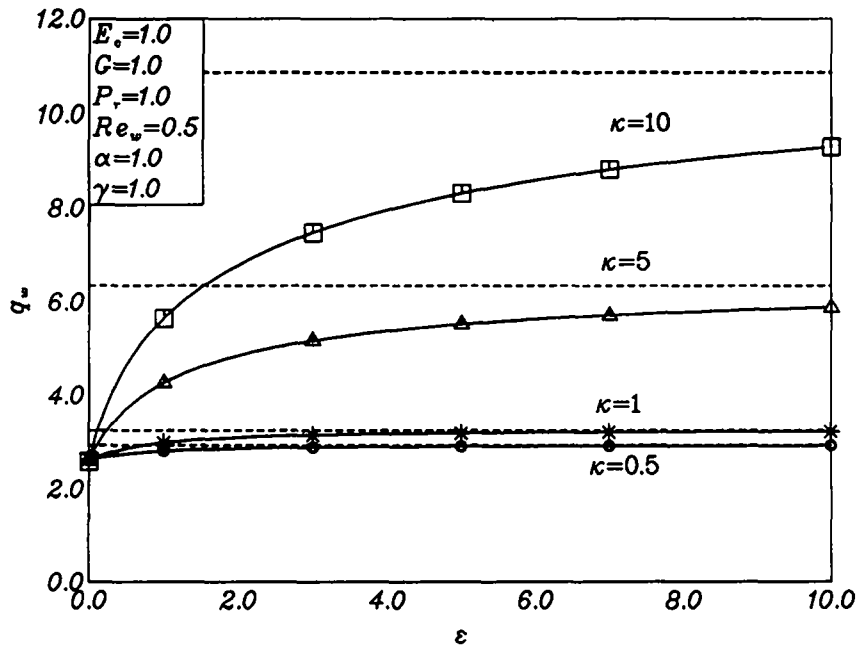

Fig. 9. Wall heat transfer coefficient vs. ϵ.

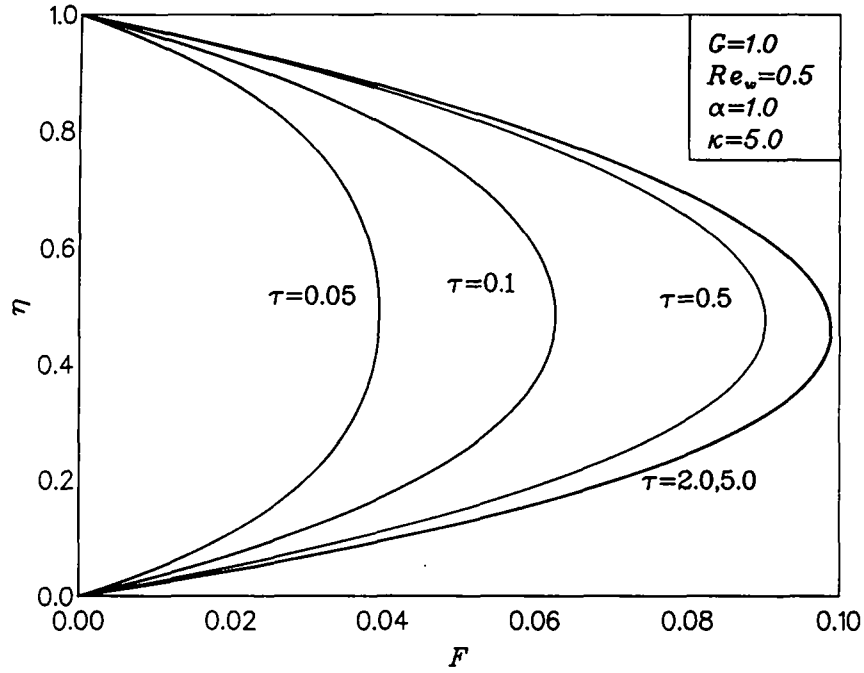

Fig. 10. Fluid-phase velocity profiles time history.

many numerical tests performed by gradually reducing the step sizes in both directions. These tests were done to insure grid independence. All derivatives with respect to τ were represented by two-point backward difference quotients. Derivatives with respect to η in the second-order equations in η [equations (2.4) and (2.6)] were represented by three-point central difference quotients while η differencing in the first-order equations in η [equations (2.5) and (2.7)] was accomplished by the trapezoidal rule. The general solution was obtained line by line starting at $\tau = 0$ and marching forward in time until steady-state conditions are reached at large values of τ. Iteration was used at each line of constant τ and a tri-diagonal matrix of linear algebraic equations was created there and solved numerically by Thomas' algorithm, as discussed by Blottner [19]. The iteration process was continued until convergence of the desired solution occurred within certain acceptable limits (when the difference between the current and the previous iteration is 10^{-5} in this case). Transient solutions for the flow fields, the temperature distributions and wall heat transfer are reported below. Many results were obtained through the course of this work. Some are shown graphically in Figs 10–17 to elucidate special features of the solutions.

Figures 10 and 11 present the development of the velocity profiles for the fluid and particle phases with time in the channel, respectively. It is seen from Fig. 10 that, in the initial time stages of the flow, the fluid-phase velocity profile is flat in the middle of the channel and more distinctive peaks occur as time progresses. Similar behavior is exhibited in the particle-phase velocity profiles shown in Fig. 11 except that the distinctive peaks occur close to the lower wall of the channel as steady-state conditions are reached at relatively large values of τ. It is also observed that particle-phase wall slip is predicted at the lower surface of the channel.

Figures 12–14 depict the behavior of the fluid-phase volume flow rate Q, the particle-phase volume flow rate Q_p, and the fluid-phase skin-friction coefficient at the lower wall C with time for various values of the particle loading κ, respectively. The dashed lines in these and all subsequent figures are associated with the steady-state values approached by the different lines. Initially, the flow is at rest, and thus Q, Q_p, and C are identically zero. As the constant pressure gradient is applied, motion of the suspension starts and the volume flow rates and the friction coefficient continue to increase until the flow stabilizes and the steady conditions are attained.

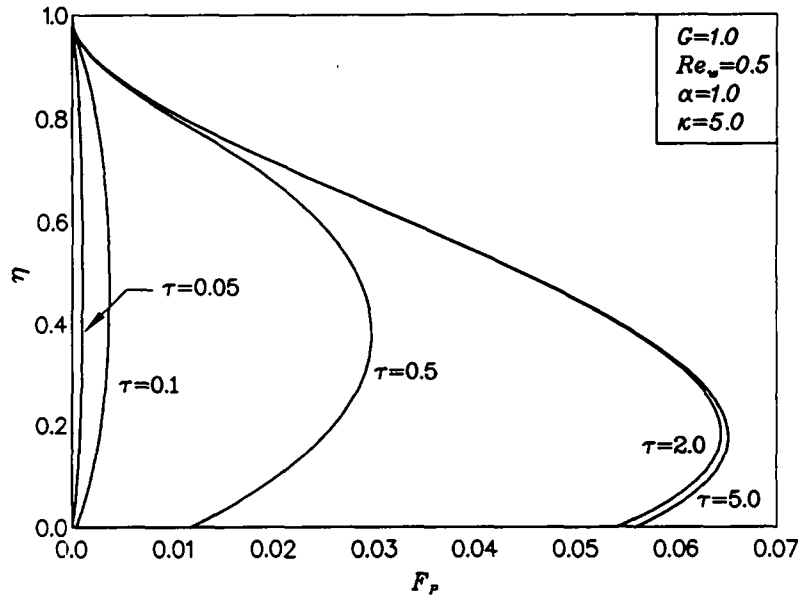

Fig. 11. Particle-phase velocity profiles time history.

This behavior is clearly shown in Figs 12–14. It should be noted that Q_p is always lower than Q for the parametric values because the particle phase is actually being dragged along by the carrier fluid phase. Increases in the particle-phase density which result in increases in the values of κ have a tendency to reduce the fluid- and particle-phase velocities in the channel and the associated fluid wall friction. This causes Q, Q_p, and C to decrease with increasing κ as evident from Figs 12–14. It is also apparent from these figures that the approach to the steady-state conditions occurs relatively quickly.

Figures 15–17 present the evolution of the fluid-phase temperature profile θ, the particle-phase temperature profile θ_p, and the wall heat transfer coefficient q_w with time, respectively. The proper transition from transient conditions at small values of τ to steady

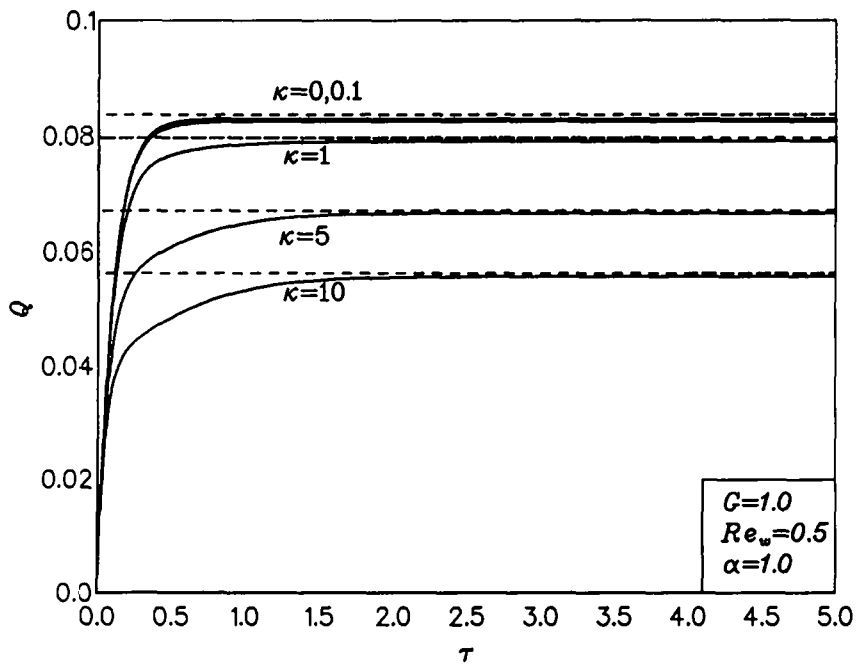

Fig. 12. Fluid-phase volume flow rate time history.

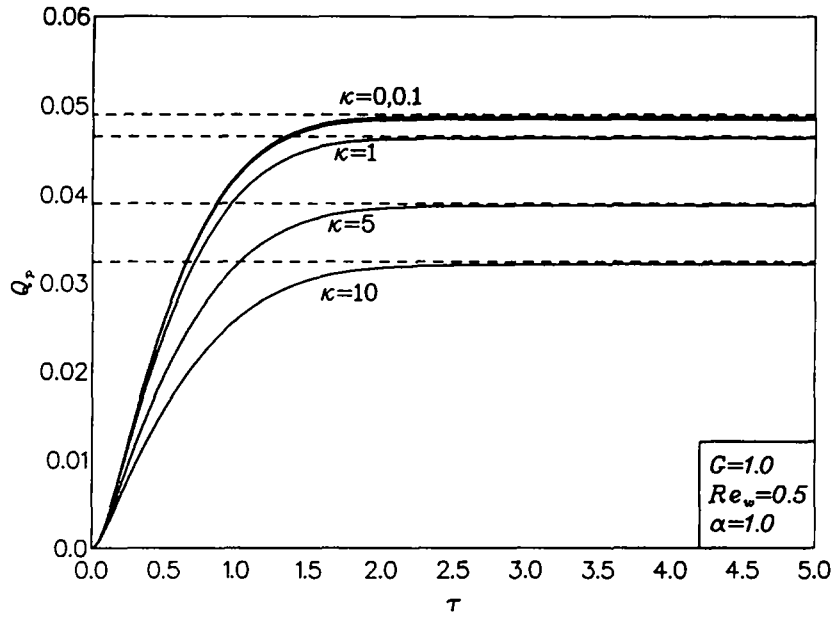

Fig. 13. Particle-phase volume flow rate time history.

conditions at large values of τ is apparent. It can be seen that lower temperatures of both phases occur in the lower portion of the channel as time progresses and, as a result, q_w decreases as τ increases until steady-state conditions are reached where no further changes in the physical variables with time take place as seen from Fig. 17. For the parametric conditions shown on Figs 15 and 16, it can be seen that large temperature differences between the phases are predicted at the lower wall of the channel. As the particle loading increases, more energy exchange between the phases takes place and the fluid phase experiences a gain in its temperature. Consequently, the heat transfer to the wall increases. This behavior is clearly evident from Fig. 17. It should be noted that the value of q_w at $\tau = 0$ is very large (since the

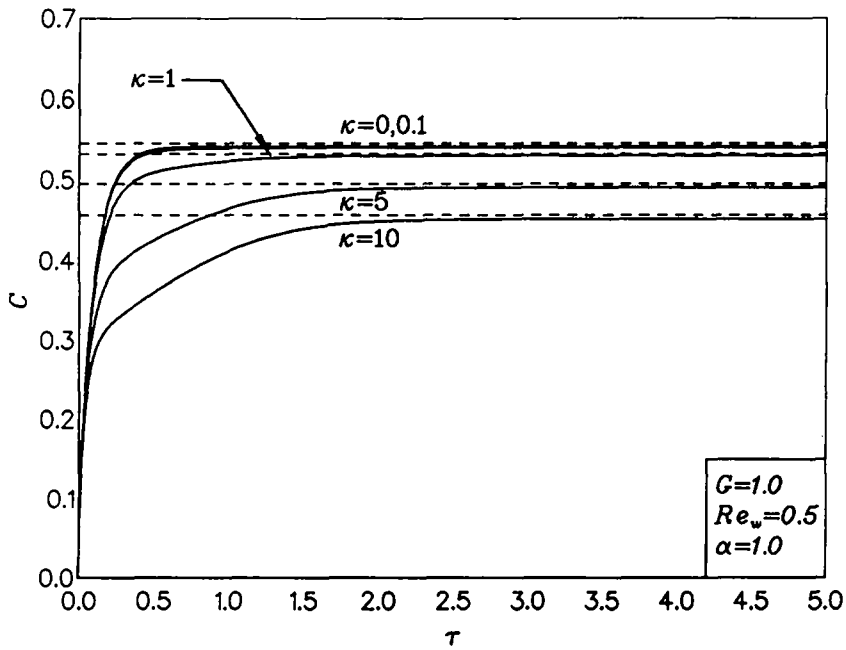

Fig. 14. Fluid-phase skin-friction coefficient time history.

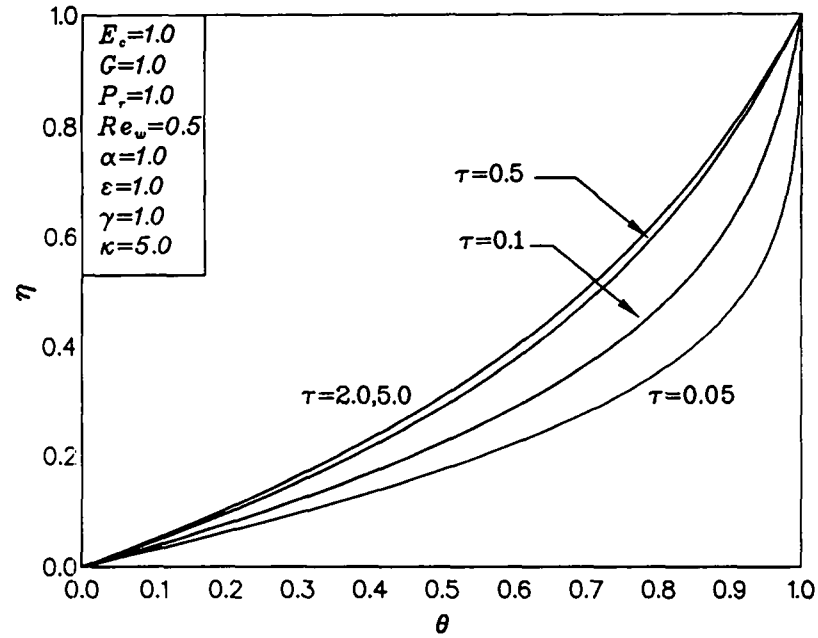

Fig. 15. Fluid-phase temperature profiles time history.

slope of the fluid-phase temperature at the lower surface of the channel is large) and lies outside the scale of the figure.

It should be mentioned that all the steady-state results associated with Figs 10–17 are in excellent agreement with the closed-form steady solutions reported earlier. This tends to confirm that the numerical method chosen to solve the present problem is adequate and that, where appropriate, the resulting solutions can be used with confidence.

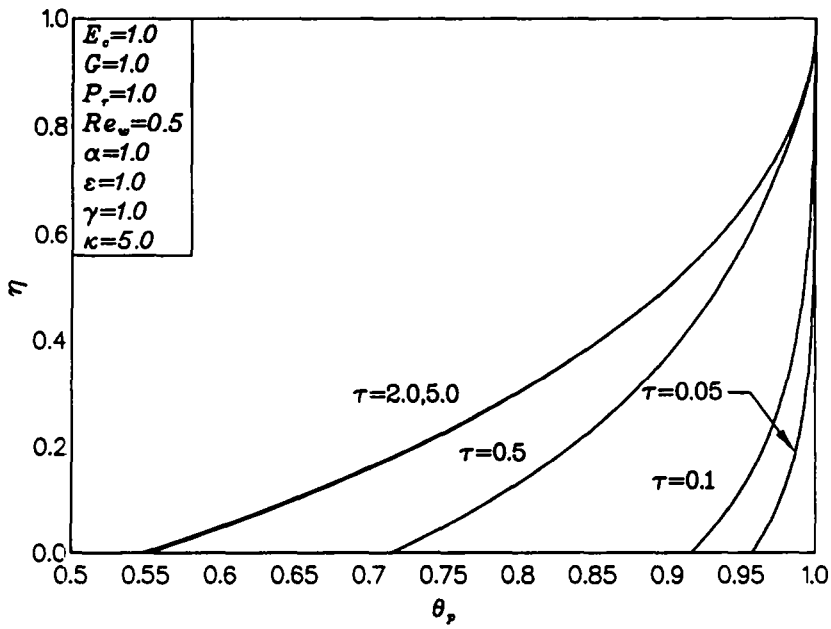

Fig. 16. Particle-phase temperature profiles time history.

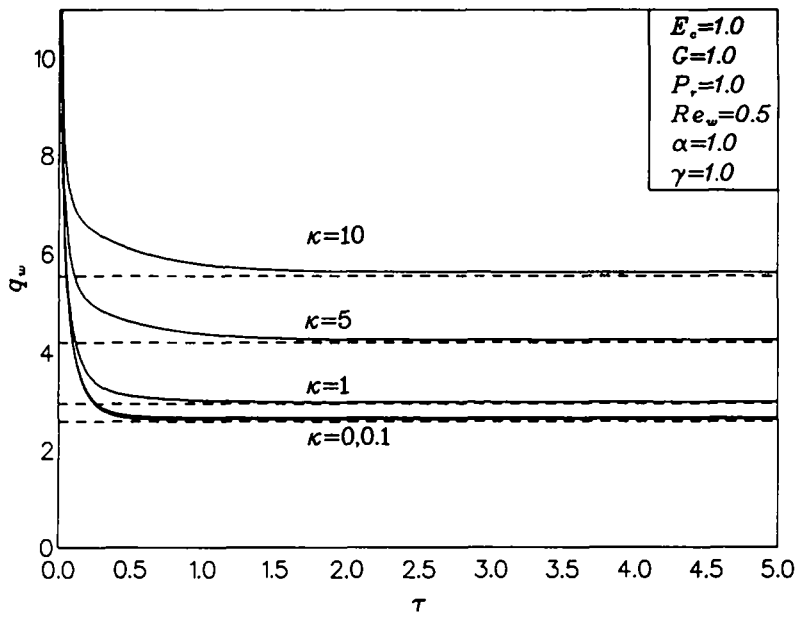

Fig. 17. Wall heat transfer coefficient time history.

4. CONCLUSION

A two-phase fluid-particle model based on the continuum approach was formulated for the problem of flow and heat transfer in a porous channel with uniform suction and injection applied at the lower and upper plates of the channel, respectively. Because of the simplicity introduced by the uniform suction and other assumptions, the steady-state version of the problem was solved in closed form. A numerical method based on the finite-difference methodology was developed to check the correctness of the analytical solutions and to be used in the solution of the transient version of the problem. Numerical evaluations of the steady analytical results were performed and compared with the corresponding numerical solutions and some graphical results were presented and discussed. As expected, the presence of particles caused lower fluid-phase velocities (and thus, lower fluid volume flow rates), higher fluid-phase temperatures, and lower wall heat transfer. Although the steady exact solutions were found to be in excellent agreement with the numerical solutions, no comparisons with experimental data were made due to the absence of such data in the literature. It is hoped that the solutions presented in this paper can be used as a stimulus for experimental work and in validating computer codes for more complex problems.

REFERENCES

[1] M. WHITE, *Viscous Fluid Flow*. McGraw Hill, New York (1974).
[2]. J.M. RITTER and J. PEDDIESON, *Proc. of the Sixth Canadian Congress of Applied Mechanics* (1977).
[3] A.J. CHAMKHA, *Int. J. Engng Sci.* **33**, 437 (1995).
[4] F.E. MARBLE, *Annual Review of Fluid Mechanics* **2**, 297 (1970).
[5] M. ISHII, *Thermo-Fluid Dynamic Theory of Two-Phase Flow*. Eyrolles, Paris (1975)
[6] W.T. SHA and S.L. SOO, *Int. J. Heat and Mass Transfer* **21**, 1581 (1978).
[7] N. ZUBER, *Chem. Engng Sci.* **19**, 897 (1964).
[8] P.G. SAFFMAN, *J. Fluid Mech.* **22** 385 (1965).
[9] S.I. RUBINOW and J.B. KELLER, *J. Fluid Mech.* **11**, 447 (1961).
[10] N.N. APAZIDIS, *Int. J. Multiphase Flow* **11**, 657 (1985).
[11] A.J. CHAMKHA, *ASME J. Heat Transfer*. In press.
[12] S.L. SOO, *Appl. Sci. Res.* **21**, 68 (1969).
[13] Y.P. TSUO and D. GIDASPOW, *AIChE J.* **36**, 885 (1990).

[14] M. GADIRAJU, J. PEDDIESON and S. MUNUKUTLA, *Mech. Res. Comm.* **19,** 7 (1992).
[15] D.A. DREW and R.T. LAHEY, *J. Fluid Mech.* **117,** 91 (1982).
[16] J.L. SINCLAIR and R. JACKSON, *AIChE J.* **35,** 1473 (1989).
[17] S.K. WANG, S.J. LEE, O.C. JONES and R.T. LAHEY, *Int. J. Multiphase Flow* **13,** 327 (1987).
[18] S.V. PATANKAR, *Numerical Heat Transfer and Fluid Flow*. McGraw-Hill, New York (1980).
[19] F.G. BLOTTNER, *AIAA J.* **8,** 193 (1970).

(Received 15 January 1994; accepted 29 January 1996)

NOMENCLATURE

c fluid-phase specific heat at constant pressure
C fluid-phase skin-friction coefficient
d particle diameter
E_c fluid-phase Eckert number
$\vec{e}_x, \vec{e}_y$ unit vectors in x and y directions, respectively
$\vec{f}$ interphase force per unit volume acting on the particle phase
F dimensionless fluid-phase axial velocity
G dimensionless fluid-phase pressure gradient
I unit tensor
$\bar{K}$ fluid-phase thermal conductivity
l channel width
p fluid-phase pressure
$\mathrm{P_r}$ fluid-phase Prandtl number
Q fluid-phase volumetric flow rate
Q_T interphase heat transfer rate per unit volume to the particle phase
q_w wall heat transfer coefficient
$\mathrm{Re_w}$ wall Reynolds number
t time
T fluid-phase temperature
T_0 lower plate temperature
T_l upper plate temperature
$\vec{V}$ fluid-phase velocity vector
V_c characteristic velocity
V_w suction or injection velocity
x,y Cartesian coordinate variables

Greek Symbols

ϵ temperature inverse Stokes number
α velocity inverse Stokes number
γ specific heat ratio
∇ gradient operator
∇^2 Laplacian operator
κ particle loading
μ fluid-phase dynamic viscosity
ϕ particulate volume fraction
ρ fluid-phase density
ρ_s density of particulate material
σ fluid-phase stress tensor
$\bar{\tau}$ dimensionless time
τ_T temperature relaxation time (= $(\rho_s d^2 c_p)/(12k)$)
τ_v Velocity relaxation time (= $(\rho_s d^2)/(18\mu)$)
θ dimensionless fluid-phase temperature
η dimensionless normal coordinate

Subscripts

p particle phase

Superscripts

T transpose of a second-order tensor